PHYSICAL REVIEW APPLIED **14,** 064042 (2020)

Editors' Suggestion

Trapped State at a Dislocation in a Weak Magnetomechanical Topological Insulator

Inbar Hotzen Grinberg,[1] Mao Lin,[2] Wladimir A. Benalcazar,[2] Taylor L. Hughes,[2,*] and
Gaurav Bahl[1,†]

[1] *Department of Mechanical Science and Engineering, University of Illinois at Urbana-Champaign, Urbana, Illinois 61801, USA*
[2] *Department of Physics, University of Illinois at Urbana-Champaign, Urbana, Illinois 61801, USA*

(Received 3 September 2020; accepted 5 October 2020; published 14 December 2020)

Topological insulators are characterized by an insulating bulk and symmetry-protected bound states on their boundaries. A "strong" topological insulator is characterized by robust conducting states on *all* boundaries protected by certain internal symmetries. A "weak" topological insulator (WTI), however, requires lattice translation symmetry, making it more sensitive to disorder. However, this sensitivity gives rise to interesting characteristics, such as anisotropic edge modes, quantized charge polarization, and bound states appearing at dislocation defects. Despite hosting interesting features, the sensitivity of WTIs to disorder poses an experimental confirmation challenge. Here we realize a two-dimensional (2D) magnetomechanical metamaterial and experimentally demonstrate the unique features of a WTI. Specifically, we show that the 2D WTI is anisotropic and hosts edge modes only on certain edges, as well as hosting a bound state at a dislocation defect. We construct the 2D WTI from stacked 1D Su-Schrieffer-Heeger chains for which we experimentally show the different gapped phases of the 1D model.

DOI: 10.1103/PhysRevApplied.14.064042

I. INTRODUCTION

Topological insulators (TIs) are bulk-insulating materials with symmetry-protected conducting states on their boundaries [1–4]. Since their discovery [5,6], the concept of TIs has expanded and they have been demonstrated in different metamaterial systems, including photonic crystals [7–10], mechanical systems [11–15] and acoustic systems [16,17]. A "strong" TI is characterized by a quantized topological invariant and hosts robust conducting states on all boundary terminations. Furthermore, the boundary states, and any observable properties dependent on the topological invariant [18,19], are protected against disorder and defects by certain discrete, internal symmetries [20–23]. Soon after the initial predictions of time-reversal invariant topological insulators, the concept of "weak" topological insulators (WTIs) was proposed [24–26]. In this context the WTIs were protected only in the presence of time-reversal symmetry and lattice translation symmetry, which makes them, in principle, more sensitive to disorder, and hence weaker. The possible classes of WTIs were extended to allow for many different types of internal symmetries, but they are all linked by the requirement for some type of lattice translation symmetry [20]. Strong TIs are characterized by quantized electromagnetic response properties that are isotropic and manifest as robust boundary states on all boundaries [19]. In contrast, since the symmetry protection of WTIs is related to lattice translation symmetry, WTIs are typically anisotropic, and exhibit low-energy boundary modes only on certain boundary terminations and orientations [24–26]. WTIs may also exhibit interesting anisotropic electromagnetic properties, e.g., quantized charge polarization [27], but again, these are only quantized in the presence of lattice translation symmetry. In addition to these two types of properties, Ran *et al.* [28] made the remarkable prediction that crystal dislocations, which are essentially symmetry fluxes for lattice translation symmetry [29–33], can trap midgap topological bound states that can be observed spectroscopically.

Let us illustrate these properties in a simple limit. All WTIs can be generated by stacking lower-dimensional strong TIs into a periodic array [24]. As an example, we take copies of a strong one-dimensional (1D) TI aligned along the x direction [Fig. 1(a)] and stack them in the y direction with equal spacing [Fig. 1(b)]. This construction generates a set of lattice lines, the 1D TI chains, parameterized by a reciprocal vector $\mathbf{G}$ that is orthogonal to the chains, and sets a stacking direction ($\mathbf{G} = (2\pi/a)\hat{v}$ for stacking in the direction of unit vector $\hat{v}$ in real space, where a is the lattice constant). The resulting WTI is protected by whichever internal symmetries required to protect the 1D strong TI as well as by lattice translation symmetry in the stacking direction. Although the WTI

---

[*] hughest@illinois.edu
[†] bahl@illinois.edu

phase remains stable when the 1D chains are coupled in the stacking direction, we can identify any interesting topological properties in the limit when the chains remain decoupled. We note that in our experiments the coupling is always nonzero; however, for the sake of clarity, we first illustrate these phenomena in this decoupled limit. The 1D TIs have end states, as a result of which the resulting 2D WTI will have edge states comprised of the stacked 1D end states on edges parallel to the y axis. However, it will not have edge states on edges parallel to the x axis, which illustrates the surface anisotropy [24]. If the 1D TI has a quantized electromagnetic property then the WTI will typically exhibit the same property, but with a coefficient that depends on the number of layers in the **G** direction [34].

To illustrate the dislocation bound state in a WTI, we can introduce an edge dislocation, which is essentially an extra partial line of sites into the system. If the partial line is parallel to the 1D TI chains [Fig. 1(c)] then the termination of this extra line, i.e., the dislocation core, will harbor a localized end state from that 1D TI. The Burgers vector **B** of such a dislocation [35] will be parallel to **G**, and, hence, if we apply the topological index theorem introduced in Ref. [28] then we can count the number of stable dislocation modes to be $n = \mathbf{G} \cdot \mathbf{B}/2\pi$ modulo 2. For the example shown in Fig. 1(c), we have $\mathbf{G} = 2\pi\hat{y}$ (setting lattice constant $a = 1$) and $\mathbf{B} = -\hat{y}$, whereas in Fig. 1(d), **G** remains the same but $\mathbf{B} = \hat{x}$. Thus, if we insert an odd (even) number of partial lattice lines, there will be one (no) protected midgap mode trapped at the dislocation core. While the picture described above provides a simple description of the interesting WTI phenomena in the decoupled limit, the remarkable thing is that it survives even when the chains are (strongly) coupled as long as the bulk gap does not close and the symmetries are preserved. Thus, we would find that the edge states that exist on the edges parallel to the y axis will couple to each other and disperse along the edge, and that the dislocation defect traps a 0D mode that is exponentially localized on the dislocation core in a 2D system. If **B** is orthogonal to **G**, however, no mode will be trapped at the dislocation defect [Fig. 1(d)].

Despite having a range of interesting features, WTIs pose a challenge to confirm experimentally due to their

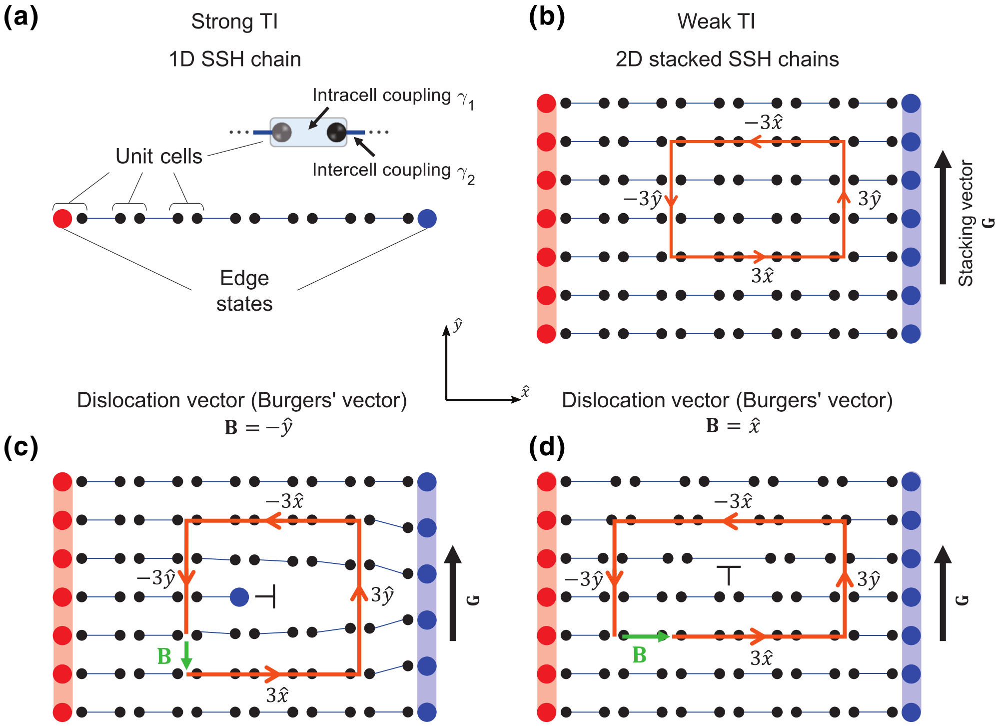

FIG. 1. (a) Illustration of a dimerized array forming a 1D topological insulator—the SSH chain. For visual simplicity, we illustrate the limiting case where intracell coupling γ_1 is zero. This 1D array exhibits two midgap states localized on the two edges. (b) A 2D WTI is formed by stacking SSH 1D TIs while preserving translation symmetry. Localized midgap modes should appear on edges that are parallel to the stacking vector **G**. In this array, starting from any point and taking N_{step} (N_{step} is an integer) steps in each direction (the step size is equal to the lattice constant for both directions) will always result in a closed path. Here we demonstrate the case with $N_{\text{step}} = 3$, and the closed path is indicated by orange arrows. Taking the same closed path around a dislocation will result in a mismatch between the beginning and end points. The Burgers vector **B** is the vector connecting these two points and characterizes the dislocation. (c) A 2D WTI with a dislocation defect having Burgers vector $\mathbf{B} = -\hat{y}$ traps a localized mode at the dislocation core. (d) A 2D WTI with a dislocation defect having Burgers vector $\mathbf{B} = \hat{x}$ does not trap a mode at the dislocation core due to orthogonality with the stacking vector **G**.

fragility to disorder [36,37], and as a result, WTIs have only recently been verified experimentally in solid-state systems [26] and photonic crystals [38,39]. Here we take another approach for the realization of WTIs using a 2D magnetomechanical metamaterial [40]. We exhibit the important spectroscopic features mentioned above, i.e., the anisotropic edge states, and the dislocation bound state. As the building block of our 2D WTI, we use a 1D Su-Schrieffer-Heeger (SSH) strong TI [41–43] composed of a dimerized chain of mechanical resonators. As a proof of concept, we first demonstrate different gapped phases of the SSH chain as well as a localized mode trapped on the domain wall between topologically trivial and nontrivial phases. We then generate a WTI by stacking the SSH chains in the transverse direction. We demonstrate the WTI anisotropy by showing the existence of edge modes in only one direction (i.e., left and right but not on top and bottom). Upon introducing a dislocation with Burgers vector orthogonal to the stacking direction, we observe a bound state trapped at the core of the dislocation which signals the nontrivial topology of the deformed lattice.

II. EXPERIMENTAL RESULTS

We experimentally implement the 1D SSH chains using an array of identical mechanical resonators coupled through magnetic interaction. Each resonator has a single rotational degree of freedom θ around the $\hat{z}$ axis and is designed to operate in its torsional resonance mode [Fig. 2(a)]. The resonance is facilitated by an aluminum serpentine spring that provides a mechanical restoring torque when $\theta \neq 0$. Each resonator has a neodymium magnet bonded to a central platform that serves as the resonating mass, while simultaneously producing a magnetic field through which adjacent resonators are coupled [44]. This magnetic field decays cubically with distance, allowing control of the coupling rates by manipulating the spacing between resonators. Each mechanical resonator is analogous to an atom and we define a unit cell as two adjacent resonators with intracell coupling γ_1. We can then arrange these unit cells with periodicity along $\hat{x}$ and $\hat{y}$ to produce desired structures.

The magnetically induced torque between dipoles introduces an additional spring effect that can either soften or stiffen the torsional mechanical stiffness of each resonator [45] depending on its local magnetic environment. Since the resonators on the ends of these arrays have only a single neighbor, they experience a different magnetostatic spring effect compared against resonators within the bulk, and as a result, their resonance frequency is detuned. We compensate for this undesirable effect with the use of fixed magnets at both ends of the array, and ensure that the frequencies across the array are as uniform as possible.

In order to measure the local magnetomechanical susceptibility (angular displacement per applied torque) of the array, we employ a frequency domain forced-response measurement. We harmonically drive each resonator with a small solenoid coil, and measure the resulting torsional oscillation as a function of frequency using a Hall sensor placed nearby [Fig. 2(a)]. The susceptibility spectrum is then calculated as the ratio of the angular amplitude to the applied torque at a given frequency. This susceptibility spectrum measured at each resonator is directly proportional to the local spectral density of states. By averaging these local measurements from all the resonators in the array we obtain the system-wide density of states, up to a proportionality factor.

The resonator arrays studied in this paper are characterized by mechanical second-order equations of motion. Using a slowly varying envelope approximation [44], we rewrite these equations to obtain the momentum space Bloch Hamiltonian. For a 1D SSH chain [Fig. 1(a)] composed of magnetomechanical resonators, having intracell coupling γ_1 and intercell coupling γ_2, this Hamiltonian reads

$$H(k_x) = \begin{bmatrix} \dfrac{\omega^2 - \omega_r^2}{2\omega} - \dfrac{ic}{2I} - \dfrac{c}{2I\omega} & \dfrac{\gamma_2}{\omega} e^{-ik_x} + \dfrac{\gamma_1}{\omega} \\ \dfrac{\gamma_2}{\omega} e^{ik_x} + \dfrac{\gamma_1}{\omega} & \dfrac{\omega^2 - \omega_r^2}{2\omega} - \dfrac{ic}{2I} - \dfrac{c}{2I\omega} \end{bmatrix}. \tag{1}$$

Here k_x is the momentum, c is a viscous damping coefficient, I is the mechanical moment of inertia, ω_r is the effective resonance frequency (including both the mechanical resonance frequency and magnetostatic spring effect [45]), and ω is the angular frequency of a harmonically oscillating solution. Note that the Hamiltonian in Eq. (1) differs from a SSH model Hamiltonian [43] only by a term proportional to the identity matrix; therefore, the eigenstates of the two are identical, and thus so are all of the topological properties.

We experimentally assembled 1D SSH chains comprised from four unit cells periodically arranged along the $\hat{x}$ direction. We demonstrate the three configurations of the SSH model corresponding to topologically trivial ($\gamma_1 > \gamma_2$), critical ($\gamma_1 = \gamma_2$), and nontrivial ($\gamma_1 < \gamma_2$) phases by adjusting the relative distances between the resonators, i.e., changing the ratio between the intercell and intracell couplings γ_2/γ_1. The measured system-wide normalized mechanical susceptibility (mechanical density of states) of these configurations is presented in Figs. 2(b)–2(d) where different response bands are highlighted. The spatial mode distribution corresponding to the highlighted regions is presented as well. For an array in the topologically trivial phase [Fig. 2(b)], two bands separated by a bandgap are obtained, as expected [43], and the states in both bands are spatially distributed almost evenly across the array. Since the magnetic coupling between resonators decays cubically with distance, next-nearest neighbor coupling is

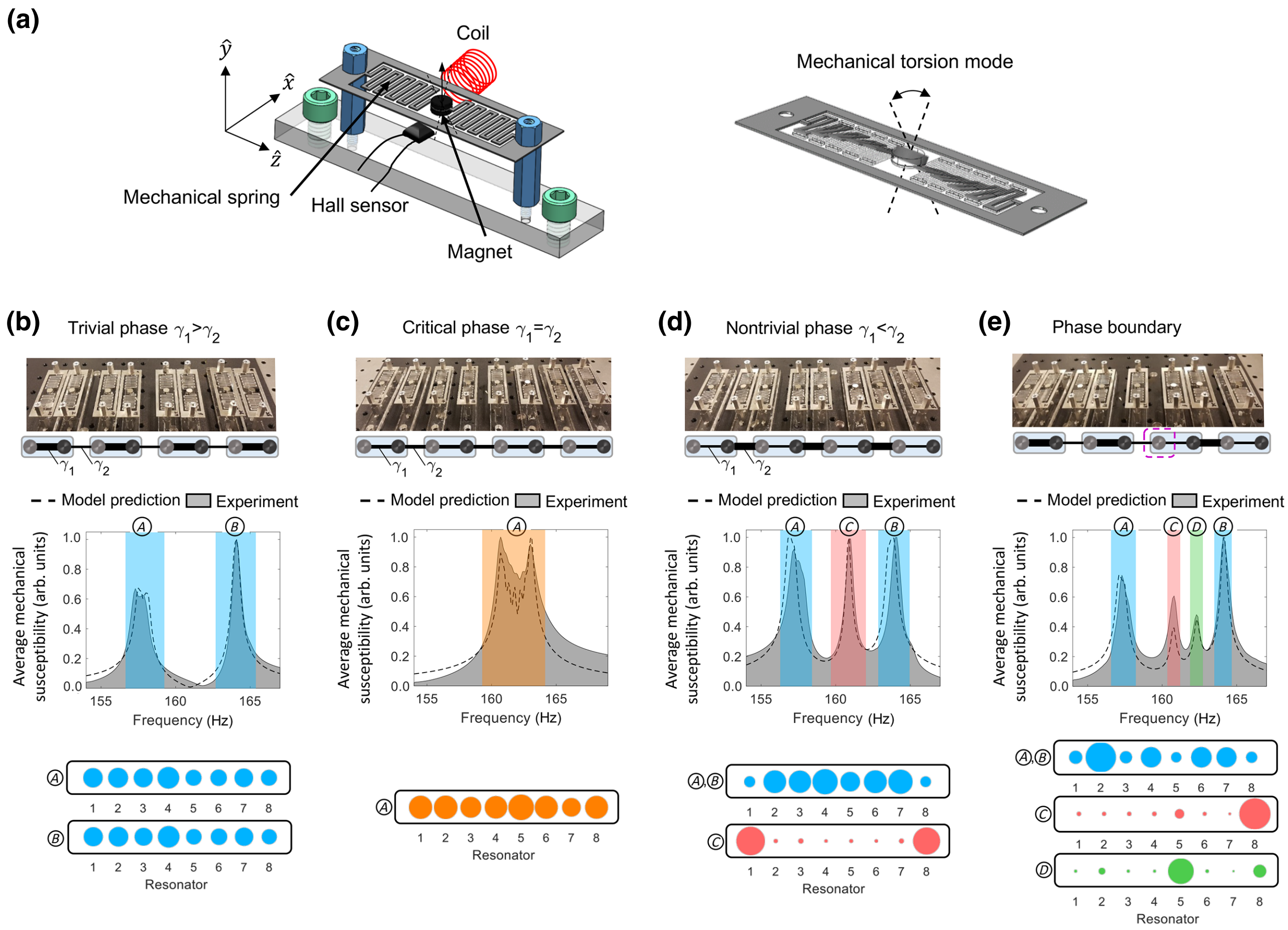

FIG. 2. (a) Illustration of a magnetomechanical resonator and its torsional resonance mode. The mechanical restoring torque is produced by an aluminum serpentine spring. A drive coil and Hall sensor are used to make local spectroscopic measurements at each resonator. We perform a series of experiments for 1D configurations of a dimerized resonator chain, corresponding to the (b) trivial phase (insulator), (c) critical point (metallic), and (d) nontrivial phase (topological insulator). (e) Demonstration of a domain wall between a trivial and a nontrivial phase. For each case in (b)–(e), we present a photograph of the experimental setup with a tight binding model illustration (thicker lines correspond to higher coupling rates). We also present experimentally measured system-wide normalized mechanical susceptibility, which is the averaged system susceptibility at each frequency and corresponds to the mechanical density of states. The dashed lines are the theoretical model predictions. Panels (b)–(e) also include the spatial distribution of states averaged over the highlighted bands (circle size corresponds to the excitation amplitude).

inherent in the system, which breaks the sublattice (chiral) symmetry. This manifests as a slight asymmetry in the height and spectral width of the two bands, even though the number of states in them is the same. For the critical configuration where the bandgap is closed [Fig. 2(c)], we observe a single band with almost uniform spatial distribution of states across the array. In the topologically nontrivial phase [Fig. 2(d)] three bands are identified. The lower and upper bands exhibit bulk modes, while the midgap band exhibits edge-localized modes, as can be clearly observed in the spatial distribution plots.

To rule out the possibility of the midgap modes arising from geometrical edge properties in our structure, we produced an additional arrangement having a domain wall between topologically trivial and nontrivial phases. This arrangement [Fig. 2(e)] is comprised of four unit cells, two of which are in the trivial phase and two in the nontrivial phase. The region between these two phases forms a domain wall and is therefore expected to exhibit a localized midgap mode. The average mechanical susceptibility measured in this system reveals four bands. The two outer bands are again observed to correspond to bulk modes, while the two states in the middle correspond to the localized modes formed at the boundaries of the topologically nontrivial phase. The frequency of the localized mode at the domain wall is slightly shifted (compared to the frequency of the mode at the right edge) due to slight differences in the local magnetostatic spring effect.

We now stack multiple SSH chains in the nontrivial phase [Fig. 2(d)] to produce a 2D WTI [as illustrated in

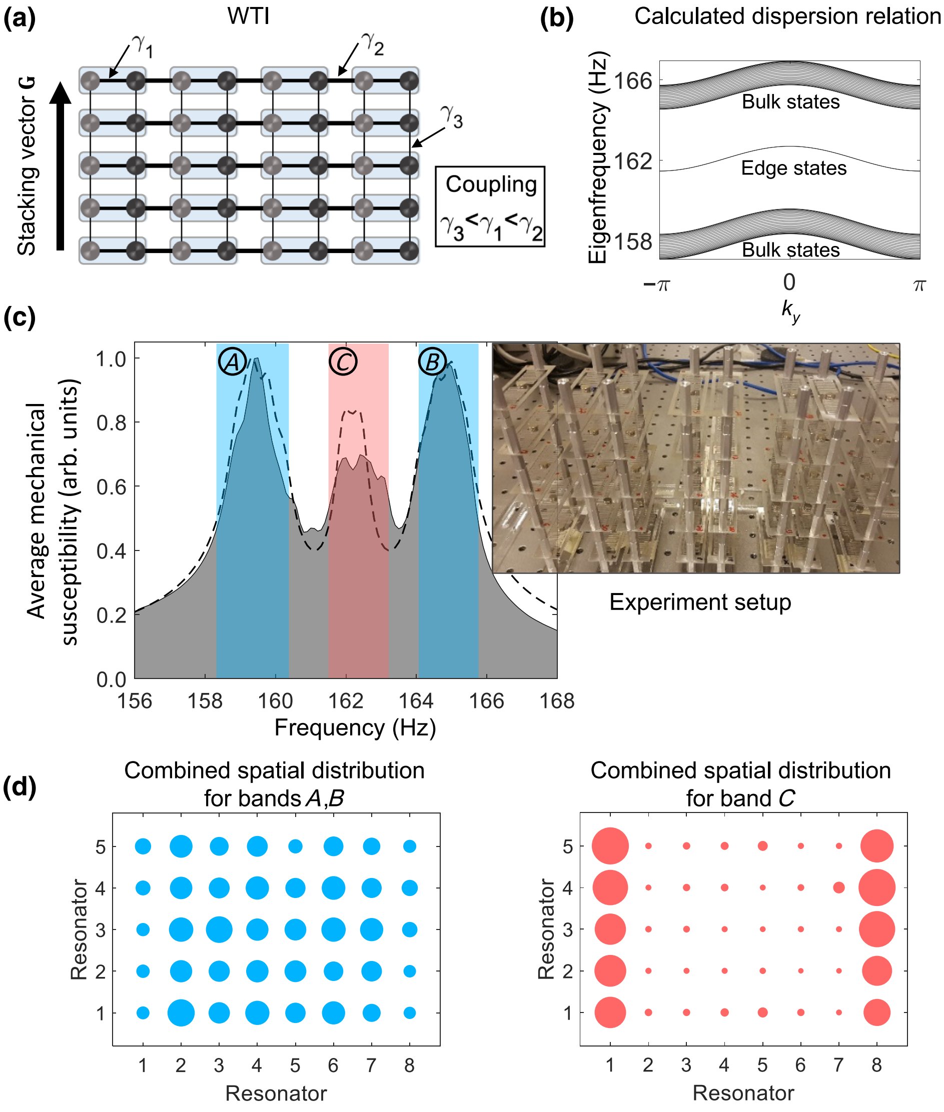

FIG. 3. (a) Schematic of a 2D WTI made from $\hat{x}$-oriented 1D SSH chains that are stacked along the $\hat{y}$ direction. The width of the coupling lines is illustrative of the coupling strength between resonators in the array ($\gamma_3 < \gamma_1 < \gamma_2$). (b) Dispersion relation calculated for a configuration similar to (a), but with 50 resonators (25 unit cells) in the $\hat{x}$ direction and the periodic boundary condition in the $\hat{y}$ direction, shows the existence of midgap modes. (c) Plot of the experimentally measured system-wide average mechanical susceptibility (normalized) versus frequency. The dashed line is the theoretical model prediction. We identify three bands of interest that are highlighted. The inset shows a photograph of the experimental setup. (d) Spatially resolved mode distribution (circle size corresponds to the excitation amplitude) over the bands identified in (c). For each resonator, the measured susceptibility is averaged over the highlighted frequency region and the circle size corresponds to the averaged magnitude. Since the response characteristics of bands A, B are similar, we combine their contributions. The lower and upper bands [A, B, blue in (c)] correspond to bulk states, while the middle band [C, pink in (c)] corresponds to the states formed on edges parallel to the stacking vector **G**.

Fig. 3(a)] with a stacking (reciprocal) vector $\mathbf{G} = 2\pi\hat{y}/d_y$, where d_y is the distance between layers in the $\hat{y}$ direction that we set to unity for convenience. The 1D TI chains are weakly and uniformly coupled along the vertical direction with coupling rate γ_3 (in our experiments we set the couplings $\gamma_3 < \gamma_1 < \gamma_2$). We have

$$H(k_x, k_y) = \begin{bmatrix} \dfrac{\omega^2-\omega_r^2}{2\omega} - \dfrac{ic}{2I} - \dfrac{c}{2I\omega} + \dfrac{2\gamma_3}{\omega}\cos k_y & \dfrac{\gamma_2}{\omega}e^{-ik_x} + \dfrac{\gamma_1}{\omega} \\ \dfrac{\gamma_2}{\omega}e^{ik_x} + \dfrac{\gamma_1}{\omega} & \dfrac{\omega^2-\omega_r^2}{2\omega} - \dfrac{ic}{2I} - \dfrac{c}{2I\omega} + \dfrac{2\gamma_3}{\omega}\cos k_y \end{bmatrix}, \tag{2}$$

where the $k_{x,y}$ are momenta along the $\hat{x}, \hat{y}$ directions, respectively [44]. In Fig. 3(b) we evaluate the dispersion relation of the 2D WTI, with periodic boundary conditions in the $\hat{y}$ direction, and open boundaries in the $\hat{x}$ direction, showing the existence of the midgap modes [34]. Because of the aforementioned anisotropy of a WTI, these midgap modes will not appear if the $\hat{x}$ direction is periodic and the $\hat{y}$ direction is open.

The measured average mechanical susceptibility of the entire 2D array [Fig. 3(c)] reveals three bands. The lower and upper bands correspond to bulk modes [left-hand plot of Fig. 3(d)], and the middle band corresponds to localized modes on the left and right edges [right-hand plot of Fig. 3(d)] as expected. The individual susceptibility measurements of all 40 resonators are available in the Supplemental Material [44].

Next, we test the occurrence of 0D midgap modes trapped at the core of a topological defect. For this, we produce a dislocation with Burgers vector $\mathbf{B} = \hat{y}$ by terminating one of the TI chains early, as shown in Fig. 4(a). The $\hat{x}$-axis positions of the resonators in the last column are then adjusted to restore translation symmetry and to roughly restore an even interchain coupling γ_3. In this configuration we expect localized modes on the left and right edges as in the case of the WTI without the dislocation, and an additional mode trapped at the dislocation core [Fig. 1(c)]. We choose three resonators as representative of the array characteristics: (I) a resonator on the left edge that is expected to have a localized mode, (II) a resonator deep inside the array that is expected to show the bulk bandgap,

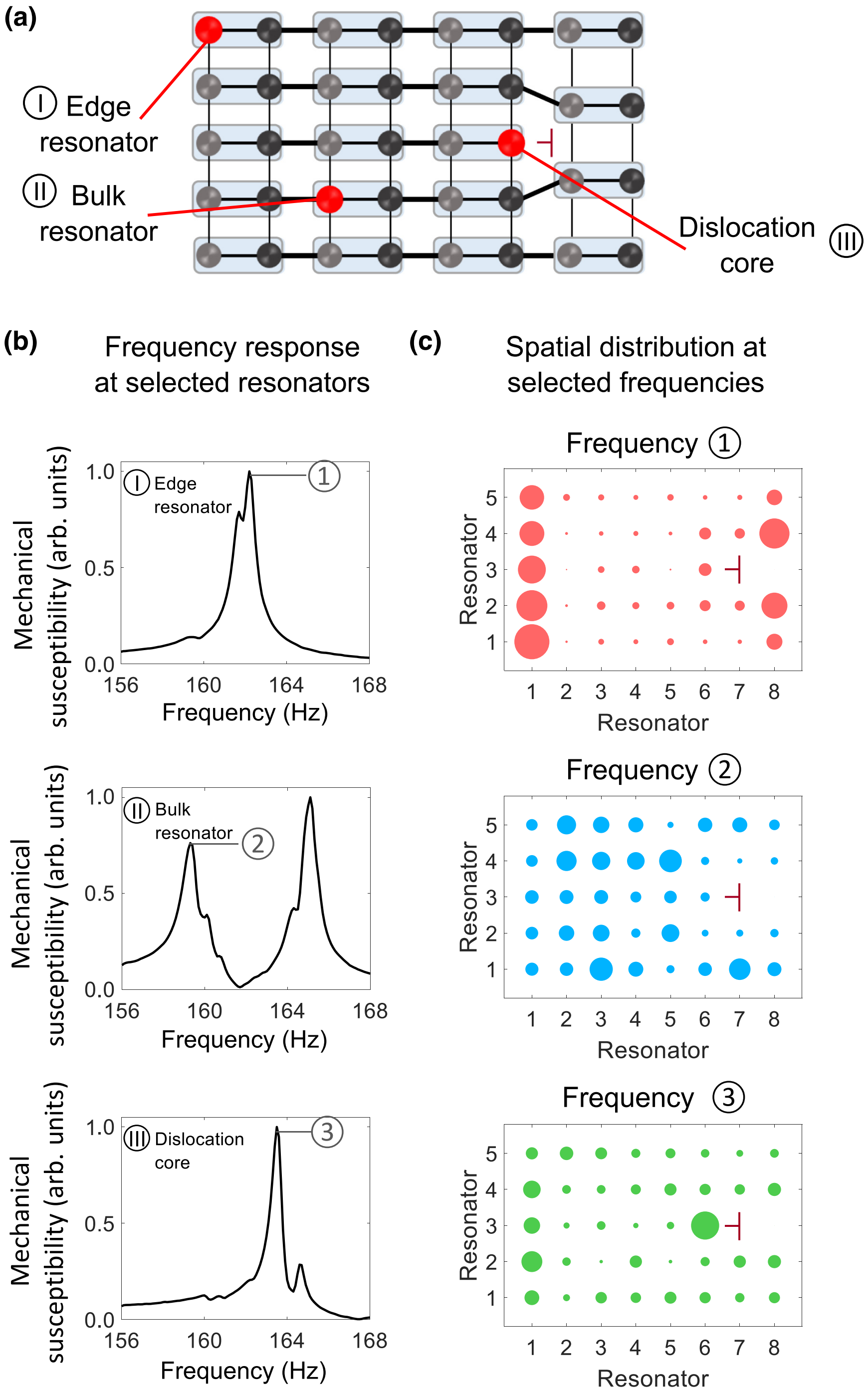

FIG. 4. Observation of a trapped mode at a dislocation defect in a 2D WTI. (a) Illustration of the 2D WTI composed of 1D TI chains (dimerized coupling) along the $\hat{x}$ direction, and approximately uniform coupling in the $\hat{y}$ direction. A unit cell is removed from the right edge of the middle row to create the dislocation defect, and the $\hat{y}$-axis positions of the last column are adjusted to compensate. Three resonators of interest (red circles) are identified. (b) The measured susceptibilities at the resonators of interest show the array characteristics and are used to identify frequencies that may correspond to states of interest. (c) Spatially resolved distribution of states at the three identified frequencies are presented, confirming the edge mode, the bulk modes, and the trapped mode at the dislocation defect.

and (III) the dislocation core that is also expected to show a localized mode. The measured normalized mechanical susceptibility of these three resonators is presented in Fig. 4(b), and matches the theoretical predictions. Once again, the individual susceptibility measurements of all 38 resonators are provided in the Supplemental Material [44]. These measurements allow us to identify frequencies of interest that should correspond to the edge mode, the bulk bands, and the dislocation defect mode. In Fig. 4(c) we present the spatial distribution of states over the entire system of 38 resonators at the identified frequencies, using the system-wide measured susceptibility. This spatial visualization confirms that the bulk and edge modes all appear as anticipated, and that the dislocation core now harbors a single trapped mode.

We note that the magnetomechanical implementation shown here is inherently disordered, e.g., resonator frequencies can only be matched within ± 0.1 Hz, which is significant compared to an approximately 2.5 Hz bandgap. The cubic dependence of magnetomechanical coupling makes the array very sensitive to variations in the inter-resonator distance, and susceptible to next-nearest neighbor coupling. In spite of this, we observe that the governing topological characteristics for WTIs still hold.

III. DISCUSSION

In this work we have presented an experimental demonstration of the anisotropic edge modes of a WTI, as well as a trapped mode at the core of a dislocation defect. These results confirm the ability of WTIs to generate both 1D and 0D topological bound states from the same 2D bulk system, which are the remarkable implications of a topological index theorem. Broadly speaking, it has been a common assumption that topological insulators protect states that are one dimension lower than that of the host material. This assumption has come to be challenged recently by the rise of high-order topological insulators [46–53] that exhibit protected states of higher codimension. Our work experimentally demonstrates yet another path to obtain lower-dimensional protected states, without relying on high-order topology. The expanded capability of producing both 0D and 1D states within the same 2D material could open up alternative avenues for robust systems, such as sensors, filters, and other signal processing devices that are resilient to disorder that might appear in manufacturing or during operation.

ACKNOWLEDGMENTS

We acknowledge funding support from the National Science Foundation Emerging Frontiers in Research and Innovation NewLAW program (Grant No. EFMA-1641084), an Office of Naval Research Director of Research Early Career Grant (Grant No. N00014-16-1-2830), and the Multidisciplinary University Research Initiative (Grant No. N00014-20-1-2325). This work is supported in part by the Zuckerman STEM Leadership Program.

[1] M. Z. Hasan and C. L. Kane, Colloquium: Topological insulators, Rev. Mod. Phys. **82**, 3045 (2010).

[2] X.-L. Qi and S.-C. Zhang, Topological insulators and superconductors, Rev. Mod. Phys. **83**, 1057 (2011).

[3] J. E. Moore, The birth of topological insulators, Nature **464**, 194 (2010).

[4] B. A. Bernevig and T. L. Hughes, *Topological Insulators and Topological Superconductors* (Princeton University Press, Princeton, 2013).

[5] B. A. Bernevig, T. L. Hughes, and S.-C. Zhang, Quantum spin hall effect and topological phase transition in hgte quantum wells, Science **314**, 1757 (2006).

[6] M. König, S. Wiedmann, C. Brüne, A. Roth, H. Buhmann, L. W. Molenkamp, X.-L. Qi, and S.-C. Zhang, Quantum spin hall insulator state in hgte quantum wells, Science **318**, 766 (2007).

[7] S. Raghu and F. D. M. Haldane, Analogs of quantum-hall-effect edge states in photonic crystals, Phys. Rev. A **78**, 033834 (2008).

[8] F. Haldane and S. Raghu, Possible Realization of Directional Optical Waveguides in Photonic Crystals with Broken Time-Reversal Symmetry, Phys. Rev. Lett. **100**, 013904 (2008).

[9] L. Lu, J. D. Joannopoulos, and M. Soljačić, Topological photonics, Nat. Photonics **8**, 821 (2014).

[10] T. Ozawa, H. M. Price, A. Amo, N. Goldman, M. Hafezi, L. Lu, M. C. Rechtsman, D. Schuster, J. Simon, O. Zilberberg, *et al.* Topological photonics, Rev. Mod. Phys. **91**, 015006 (2019).

[11] C. Kane and T. Lubensky, Topological boundary modes in isostatic lattices, Nat. Phys. **10**, 39 (2014).

[12] S. D. Huber, Topological mechanics, Nat. Phys. **12**, 621 (2016).

[13] K. Bertoldi, V. Vitelli, J. Christensen, and M. van Hecke, Flexible mechanical metamaterials, Nat. Rev. Mater. **2**, 17066 (2017).

[14] L. M. Nash, D. Kleckner, A. Read, V. Vitelli, A. M. Turner, and W. T. Irvine, Topological mechanics of gyroscopic metamaterials, Proc. Natl. Acad. Sci. **112**, 14495 (2015).

[15] N. P. Mitchell, L. M. Nash, D. Hexner, A. M. Turner, and W. T. Irvine, Amorphous topological insulators constructed from random point sets, Nat. Phys. **14**, 380 (2018).

[16] Z. Yang, F. Gao, X. Shi, X. Lin, Z. Gao, Y. Chong, and B. Zhang, Topological Acoustics, Phys. Rev. Lett. **114**, 114301 (2015).

[17] X. Zhang, M. Xiao, Y. Cheng, M.-H. Lu, and J. Christensen, Topological sound, Commun. Phys. **1**, 97 (2018).

[18] D. Xiao, M.-C. Chang, and Q. Niu, Berry phase effects on electronic properties, Rev. Mod. Phys. **82**, 1959 (2010).

[19] X.-L. Qi, T. L. Hughes, and S.-C. Zhang, Topological field theory of time-reversal invariant insulators, Phys. Rev. B **78**, 195424 (2008).

[20] A. Kitaev, Periodic table for topological insulators and superconductors, AIP Conf. Proc. 1134, 22 (2009).

[21] A. P. Schnyder, S. Ryu, A. Furusaki, and A. W. Ludwig, Classification of topological insulators and superconductors in three spatial dimensions, Phys. Rev. B **78**, 195125 (2008).

[22] C.-K. Chiu, J. C. Teo, A. P. Schnyder, and S. Ryu, Classification of topological quantum matter with symmetries, Rev. Mod. Phys. **88**, 035005 (2016).

[23] S. Ryu, A. P. Schnyder, A. Furusaki, and A. W. Ludwig, Topological: Insulators and superconductors: Tenfold way and dimensional hierarchy, New J. Phys. **12**, 065010 (2010).

[24] L. Fu, C. L. Kane, and E. J. Mele, Topological Insulators in Three Dimensions, Phys. Rev. Lett. **98**, 106803 (2007).

[25] L. Fu and C. L. Kane, Topological insulators with inversion symmetry, Phys. Rev. B **76**, 045302 (2007).

[26] R. Noguchi, T. Takahashi, K. Kuroda, M. Ochi, T. Shirasawa, M. Sakano, C. Bareille, M. Nakayama, M. Watson, K. Yaji, *et al.*, A weak topological insulator state in quasi-one-dimensional bismuth iodide, Nature **566**, 518 (2019).

[27] S. T. Ramamurthy and T. L. Hughes, Patterns of electromagnetic response in topological semimetals, Phys. Rev. B **92**, 085105 (2015).

[28] Y. Ran, Y. Zhang, and A. Vishwanath, One-dimensional topologically protected modes in topological insulators with lattice dislocations, Nat. Phys. **5**, 298 (2009).

[29] J. C. Teo and C. L. Kane, Topological defects and gapless modes in insulators and superconductors, Phys. Rev. B **82**, 115120 (2010).

[30] J. C. Teo and T. L. Hughes, Topological defects in symmetry-protected topological phases, Annu. Rev. Condens. Matter Phys. **8**, 211 (2017).

[31] R.-J. Slager, A. Mesaros, V. Juričić, and J. Zaanen, Interplay between electronic topology and crystal symmetry: Dislocation-line modes in topological band insulators, Phys. Rev. B **90**, 241403 (2014).

[32] V. Juričić, A. Mesaros, R.-J. Slager, and J. Zaanen, Universal Probes of Two-Dimensional Topological Insulators: Dislocation and π Flux, Phys. Rev. Lett. **108**, 106403 (2012).

[33] R.-J. Slager, The translational side of topological band insulators, J. Phys. Chem. Solids **128**, 24 (2019).

[34] M. Franz and L. Molenkamp, *Topological Insulators* (Elsevier, San Diego, 2013), Vol. 6.

[35] A dislocation defect in the lattice is characterized by a mismatch between the beginning and end points when tracing a closed loop of lattice translations around the dislocation core [54]. The vector connecting the end and start points is Burgers vector **B** indicating the amount of translation in units of the lattice constant.

[36] C. Pauly, B. Rasche, K. Koepernik, M. Liebmann, M. Pratzer, M. Richter, J. Kellner, M. Eschbach, B. Kaufmann, L. Plucinski, *et al.*, Subnanometre-wide electron channels protected by topology, Nat. Phys. **11**, 338 (2015).

[37] H. Hamasaki, Y. Tokumoto, and K. Edagawa, Dislocation conduction in Bi-Sb topological insulators, Appl. Phys. Lett. **110**, 092105 (2017).

[38] Y. Yang, Z. Gao, H. Xue, L. Zhang, M. He, Z. Yang, R. Singh, Y. Chong, B. Zhang, and H. Chen, Realization of a three-dimensional photonic topological insulator, Nature **565**, 622 (2019).

[39] F.-F. Li, H.-X. Wang, Z. Xiong, Q. Lou, P. Chen, R.-X. Wu, Y. Poo, J.-H. Jiang, and S. John, Topological light-trapping on a dislocation, Nat. Commun. **9**, 2462 (2018).

[40] I. H. Grinberg, M. Lin, C. Harris, W. A. Benalcazar, C. W. Peterson, T. L. Hughes, and G. Bahl, Robust temporal pumping in a magneto-mechanical topological insulator, Nat. Commun. **11**, 974 (2020).

[41] W.-P. Su, J. Schrieffer, and A. Heeger, Solitons in Polyacetylene, Phys. Rev. Lett. **42**, 1698 (1979).

[42] A. J. Heeger, S. Kivelson, J. Schrieffer, and W.-P. Su, Solitons in conducting polymers, Rev. Mod. Phys. **60**, 781 (1988).

[43] W.-P. Su, J. Schrieffer, and A. Heeger, Soliton excitations in polyacetylene, Phys. Rev. B **22**, 2099 (1980).

[44] See Supplemental Material at http://link.aps.org/supplemental/10.1103/PhysRevApplied.14.064042 for a derivation of the equations of motion, the Bloch Hamiltonians, the topological invariant, as well as the measured spectra of the system.

[45] I. H. Grinberg, A. Mangu, C. W. Peterson, E. Wilken-Resman, J. T. Bernhard, and G. Bahl, Magnetostatic spring softening and stiffening in magneto-mechanical resonator systems, IEEE Trans. Magn. **55**, 1 (2019).

[46] C. W. Peterson, W. A. Benalcazar, T. L. Hughes, and G. Bahl, A quantized microwave quadrupole insulator with topologically protected corner states, Nature **555**, 346 (2018).

[47] W. A. Benalcazar, B. A. Bernevig, and T. L. Hughes, Electric multipole moments, topological multipole moment pumping, and chiral hinge states in crystalline insulators, Phys. Rev. B **96**, 245115 (2017).

[48] W. A. Benalcazar, B. A. Bernevig, and T. L. Hughes, Quantized electric multipole insulators, Science **357**, 61 (2017).

[49] S. Imhof, C. Berger, F. Bayer, J. Brehm, L. W. Molenkamp, T. Kiessling, F. Schindler, C. H. Lee, M. Greiter, T. Neupert *et al.*, Topolectrical-circuit realization of topological corner modes, Nat. Phys. **14**, 925 (2018).

[50] M. Serra-Garcia, V. Peri, R. Süsstrunk, O. R. Bilal, T. Larsen, L. G. Villanueva, and S. D. Huber, Observation of a phononic quadrupole topological insulator, Nature **555**, 342 (2018).

[51] J. Noh, W. A. Benalcazar, S. Huang, M. J. Collins, K. P. Chen, T. L. Hughes, and M. C. Rechtsman, Topological protection of photonic mid-gap defect modes, Nat. Photonics **12**, 408 (2018).

[52] X. Ni, M. Weiner, A. Alu, and A. B. Khanikaev, Observation of higher-order topological acoustic states protected by generalized chiral symmetry, Nat. Materials **18**, 113 (2019).

[53] H. Xue, Y. Yang, G. Liu, F. Gao, Y. Chong, and B. Zhang, Realization of an Acoustic Third-Order Topological Insulator, Phys. Rev. Lett. **122**, 244301 (2019).

[54] C. Kittel, *Introduction to Solid State Physics* (Wiley, New York, 1976), Vol. 8.